

Computational Aerodynamics Study of the Lift+Cruise VTOL Concept Vehicle Components

Seyedeh Sheida Hosseini
Research Aerospace Engineer
NASA Ames Research Center
Moffett Field, CA, USA

Andrew M. Chuen*
Pathways Intern
NASA Ames Research Center
Moffett Field, CA, USA

William M. Chan
Computer Scientist
NASA Ames Research Center
Moffett Field, CA, USA

ABSTRACT

This paper describes a building-block approach for high-fidelity computational fluid dynamic simulations of NASA's Lift+Cruise (L+C) Vertical Take-off and Landing (VTOL) concept vehicle. The Reynolds-Averaged Navier-Stokes (RANS) equations are solved on overset structured grids using OVERFLOW. For these analyses, overset meshes are generated using recently developed automated meshing tools. A baseline study is initially performed on the vehicle fuselage with wings and tails. Vehicle components such as pylons and gears are then added individually and together to study incremental component aerodynamic effects. The results from this study are also used to demonstrate the capabilities of the automatic meshing tools for performing rapid computational analyses.

NOTATION

C_L	Lift coefficient
C_D	Drag coefficient
C_M	Pitching moment coefficient
$C_{L_{roll}}$	Rolling moment coefficient
C_N	Yawing moment coefficient
C_p	Pressure coefficient
M_∞	Freestream Mach number
V_∞	Freestream velocity
Re	Reynolds number
T_∞	Freestream temperature
h	Altitude
α	Angle of attack
Δ	Difference between two values
Δs_{max}	Max surface mesh spacing
Δs_{wall}	Initial wall normal spacing
y^+	Non-dimensionalized wall normal spacing

INTRODUCTION

In recent years, interest has been growing in the development of advanced air mobility (AAM) vehicles, which can provide an alternative form of transportation of people and cargo in both urban and rural areas. One subset of AAM is urban air mobility (UAM), where such vehicles operate in highly urban and suburban areas. In order to develop such vehicles, increased automation and innovative propulsion systems will be necessary, and vertical takeoff and landing (VTOL) capabil-

ity will be essential (Ref. 1). To this end, the NASA Revolutionary Vertical Lift Technology (RVLT) project is developing several UAM VTOL concept vehicle designs to guide aircraft development and focus research activities (Ref. 2).

One such concept vehicle that is currently under development is the Lift+Cruise VTOL aircraft (Ref. 3), shown in Figure 1. This vehicle consists of separate propulsion systems for vertical lift and fixed-wing cruise flight. The rotors for VTOL are mounted on pylons parallel to the longitudinal axis, and are only used for VTOL and low speed forward flight maneuvers. In cruise flight, a pusher-propeller in the rear provides thrust while the wing-mounted rotors are locked and aligned with the flow.

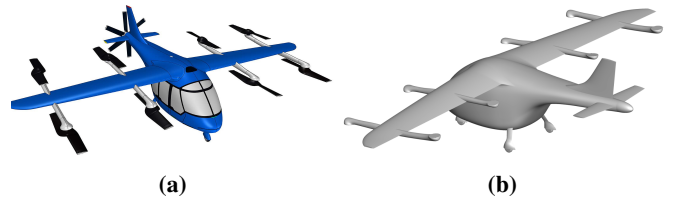


Figure 1: Geometry of the Lift+Cruise configuration. (a) Rendering of the concept vehicle. (b) Geometry of analyzed full configuration (note the lack of lifting rotors and tail propeller blades).

The numerous components suggest complex aerodynamic behavior as well as increased parasitic drag. However, to date, the characterization of the aerodynamics in the literature is still expectedly limited for the nascent concept vehicle. Johnson and Silva (Ref. 4) performed medium-fidelity comprehensive analysis of the concept vehicle. Bacchini et al (Ref. 5) performed wind tunnel tests on a small recreational drone with lift+cruise elements to quantify the drag penalty of the VTOL propulsion system in cruise flight. The experiment showed that stowing away the VTOL propellers can reduce

*Graduate Student Researcher, Department of Mechanical and Aerospace Engineering, University of California, Davis, CA, USA.

Presented at the Vertical Flight Society's 6th Decennial Aeromechanics Specialists' Conference, Santa Clara, CA, Feb. 6-8, 2024. This material is declared a work of the U.S. Government and is not subject to copyright protection in the United States.

drag by 38%, and that doing so can improve performance estimates for the scaled-up passenger-carrying aircraft. More recently, Yi et al (Ref. 6) performed high fidelity simulations of the concept vehicle during hover and transition to cruise. In that study, the unsteady Reynolds Averaged Navier-Stokes (RANS) equations, computed using the FUN3D unstructured CFD solver (Ref. 7), were loosely-coupled with the CAMDRAD-II (Ref. 8) comprehensive analysis code to perform the flow simulations. These results were mainly used to demonstrate the comparable capabilities of the SA-neg-R turbulence model to the more standard SA-neg-RC turbulence model in FUN3D. The scarcity of literature underscores the need for continued investigations of the vehicle aerodynamics and performance.

Accurate analysis of rotorcraft vehicles continues to be a complex task. The flows are highly unsteady and complex, and there may be numerous interactions between the flows around the various vehicle components. Computational fluid dynamics (CFD), specifically RANS and/or Large-Eddy Simulation (LES), can perform the necessary high-fidelity analysis to tackle this challenging problem. In particular, structured overset flow simulations are well-suited for this type of simulation, and has been used extensively for this application in the literature (Refs. 9–13). A major impediment of the analysis procedure, however, is generating a suitable near-body mesh. This process can require a significant amount of manual work depending on the complexity of the geometry. Recent efforts (Refs. 14, 15) have allowed for a semi-automatic approach for generating structured overset meshes from a Boundary Representation (BRep) geometry. This procedure can produce comparable meshes and flow-solution results when compared to the typical manual mesh process, and shows promise for reducing the manual effort required in overset CFD analysis (Ref. 16).

The focus of the current work is to characterize the flow around the Lift+Cruise VTOL concept vehicle without rotors or propellers (shown in Figure 1b) through high-fidelity simulations. Specifically, we take a building-block approach to analyze the effects of the pylons and landing gears on the vehicle aerodynamics. To perform this analysis, we use OVERFLOW (Ref. 17) to solve the RANS equations, and the aforementioned semi-automatic mesh generation approach is used to generate the near-body meshes. The remainder of the paper is structured as follows. An overview of the numerical approach is provided, including the semi-automated grid generation procedure and the flow computation procedure. A discussion of the computational studies is then presented to show the outcomes of the CFD analysis.

NUMERICAL APPROACH

Automatic Grid Generation Procedure

A semi-automatic grid generation procedure is used to generate the overset grids from a BRep solid model. This is accomplished through the following five steps: (1) surface domain decomposition, (2) surface mesh generation, (3) volume

mesh generation, (4) hole-cutting and domain connectivity computation, and (5) input generation for component aerodynamic loads computation and flow solver. Currently, these steps are performed by two modules in development within the Chimera Grid Tools (CGT) (Ref. 18) software package: EGADS2SRF and the Preprocessor for Overset Grid Simulations (POGS) (Ref. 15). The user simply has to supply global parameters on the maximum near-body edge spacing (Δs_{max}), maximum surface mesh turning angle, minimum number of points across a surface (np_{min}), maximum stretching ratio, and initial wall spacing (Δs_{wall}). Then, the two tools will create the surface and volume meshes based on these parameters.

EGADS2SRF is used to query the BRep CAD solid model through the EGADS API (Ref. 19) and to discretize the face, edge, and node entities. Here, the meshes on CAD faces, which form a subset of the final set of near-body meshes, are generated and locally refined according to the global meshing parameters provided by the user. The outputs are then fed to POGS for further processing. This step requires only a few minutes to complete.

POGS then performs Steps (1),(2),(3), and (5). In Step (2), the edge curves are used to generate edge and node surface meshes that bound and trim the various face meshes, resulting in an overset surface mesh of the geometry consisting of face, edge, and node meshes. This step also applies local refinement and stretching of these meshes as guided by the meshing parameter inputs. Automatic domain connectivity is also performed on the surface mesh to verify that the near-body generated overset system has sufficient overlap. The input files and hole-cutting instructions for the OVERFLOW flow solver are also generated at this stage (Step (5)), since only knowledge of the surface and topology is necessary for this process. It should also be noted that the auto-meshing tools produce significantly more meshes that represent the near-body region compared to meshes that are manually generated. This is due to the fact that a mesh is generated for nearly every face, edge, and node from the BRep solid. However, it has recently been shown (Ref. 16) that this has minimal effect on the integrated aerodynamic loads or efficiency of computing a solution when compared to a manually generated mesh. The surface meshing step also only requires a few minutes to complete for larger configurations.

Once the surface meshes are generated, POGS proceeds to generate the volume meshes in Step (3). The stretching and refinement in the normal direction are automatically set based on the input parameters such as the stretching ratio, the initial wall spacing, and the global max spacing. At this point, the Loosely-Coupled Boundary Conditions (LCBC) can also be applied to ensure that the volume meshes are generated together and maintain their overlap as they are marched away from the geometry surface. This process takes the most time at approximately 1-3 hours. Recent developments in the auto-meshing tools that have occurred during the writing of this paper have also enabled for more robust mesh generation for volume meshes with concave initial surfaces. A small subset of volume meshes, however, will still require additional manual repairs to eliminate any negative Jacobians or to improve

the overlap between meshes. The time required for the manual repairs is usually a few hours to 1-2 days depending on the extent of the repairs.

The final step prior to running a flow solution is to perform domain connectivity. This is still largely a manual process, and may require some iteration with the manual volume mesh repair step depending on the quality of the connectivity. For the purposes of this study, hole-cutting for the overset meshes is done through the XRAYs hole cutting approach (Ref. 20) within OVERFLOW. This step involves generating hole-cutter surfaces to “cut” or blank various parts of the volume mesh. At a minimum, a cutter for the near-body volume meshes is generated to cut the off-body meshes. Additional cutters may also be needed to ensure overlap occurs at optimal locations or to cut near-body meshes in junction regions. These cutters are usually generated from the output surface meshes from EGADS2SRF. Depending on the complexity of the grid system, this step requires approximately an hour to several days to complete for a user with an intermediate level of experience with mesh generation.

Flow Computation Procedure

The OVERFLOW 2.4a CFD code (Ref. 17) is used to compute the flow field. OVERFLOW is a flow solver that computes solutions to the three-dimensional RANS equations on structured overset grids. Modules within the code also enable additional pre-processing steps such as off-body grid generation, hole-cutting of grids, and domain connectivity. A variety of solver and discretization options are available within the code, as well as various turbulence modeling options.

For the purposes of this study, the following flow solver options were chosen. For the spatial discretization, the Roe scheme with third-order discretization and Koren limiter is used. To model the turbulence, the Spalart-Allmaras (SA) model with rotation/curvature correction (RC) is applied. The solutions are advanced with the unfactored symmetric successive over-relaxation scheme (SSOR) until convergence is detected based on best practices (Ref. 21). This is defined to be when the residuals exhibit at least a five-order magnitude drop, and the integrated force and moment coefficients converge such that the lift varies within 0.01, drag within 0.0001 (or 1 drag count) and pitching moment within 0.001. All force and moment coefficients are normalized by the reference wing area, which is 270.2 [ft²].

COMPUTATIONAL STUDIES

A computational study on the incremental aerodynamic analysis of the Lift+Cruise airframe components without rotors or propellers is performed at cruise conditions. Table 1 outlines the flow conditions considered. This computational study consists of two parts. The first aspect is to perform a grid resolution study to determine the automatic meshing inputs to produce a sufficient resolution for characterizing the aerodynamics. This is done with the “Baseline” case, which consists of the fuselage, wings, and empennage. The second part

of the study quantifies the effects of the incremental changes on the vehicle aerodynamics and the associated required resources. Various different configurations are investigated regarding how the aerodynamic behavior changes in relation to the “Baseline” case.

Table 1: Flight conditions for the Lift+Cruise concept vehicle at cruise.

Flow Parameter	English	Metric
h	5000 [ft]	1524 [m]
T_∞	77.2°F	ISA + 20°C
V_∞	80 knots	41.16 m/s
α	0.0°	0.0°

GRID RESOLUTION STUDY

Previous studies on multiple complex geometries have demonstrated that automatic meshes can produce similarly converged solutions to the manual meshes (Ref. 16). Grid resolution studies using automatic meshes were also performed on some of these geometries. For the component study in this paper, a grid resolution study on the “Baseline” configuration is revisited to establish a baseline configuration. Coarse, medium, fine, and extra-fine meshes are generated where the meshing parameters are chosen such that the grids are refined by a factor of 1.5 in each direction between subsequent levels. Table 2 summarizes the grid specifications. This family of grids is depicted in Figure 2. The parameter y^+ , which describes the non-dimensional wall distance for wall-bounded flows, is approximately 0.3 at the initial wall-normal spacing Δs_{wall} for the medium resolution. For all grid levels, it is less than one.

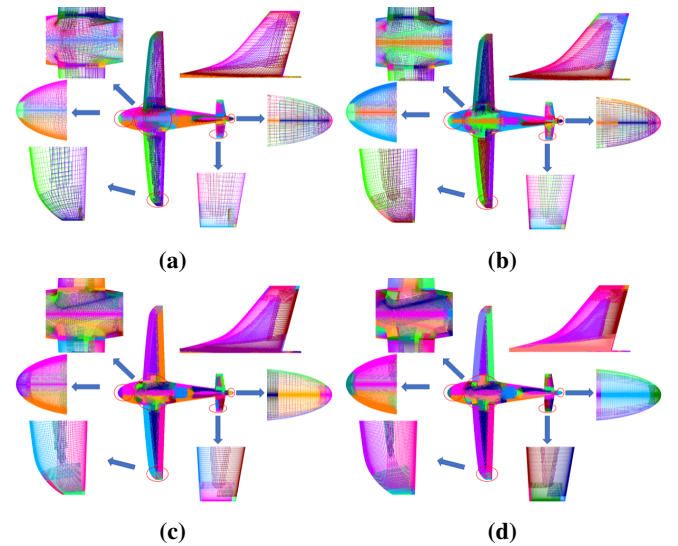


Figure 2: Family of automatic grids for the grid convergence study. (a) Coarse: 98 meshes. (b) Medium: 98 meshes. (c) Fine: 102 meshes. (d) Extra fine: 107 meshes.

Table 2: Mesh family input parameters for automatic mesh tools.

	Coarse	Medium	Fine	Extra-Fine
Number of surface points	108k	173k	351k	711k
Number of near-body volume points	5.1M	11.4M	33.7M	96.0M
Maximum stretching ratio	1.30	1.20	1.13	1.09
Maximum grid spacing [ft]	0.75	0.50	0.33	0.22
Maximum grid turning angle [deg.]	5.0	4.0	3.0	2.0
Viscous wall spacing [ft]	9.30×10^{-6}	6.15×10^{-6}	4.10×10^{-6}	2.73×10^{-6}

Table 3 shows a comparison of the converged integrated loads, which are non-dimensionalized by the wing reference area of 270.2 [ft^2]. Figure 3 demonstrates how the integrated loads evolve as the grid is refined. The aerodynamic values are plotted in black, while the linear trends are shown in red. The linear trends indicate a second-order convergence behavior as the grid is refined, and the y intercepts of the linear trends show the theoretical values on an infinite grid. The theoretical values can be used to identify the minimum sufficient resolution within an acceptable solution tolerance.

Table 3: Load coefficient comparisons across grid levels.

	C_L	C_D	C_M
Coarse	0.163	0.02736	-0.0531
Medium	0.161	0.02589	-0.0480
Fine	0.159	0.02462	-0.0442
Extra-fine	0.157	0.02368	-0.0419

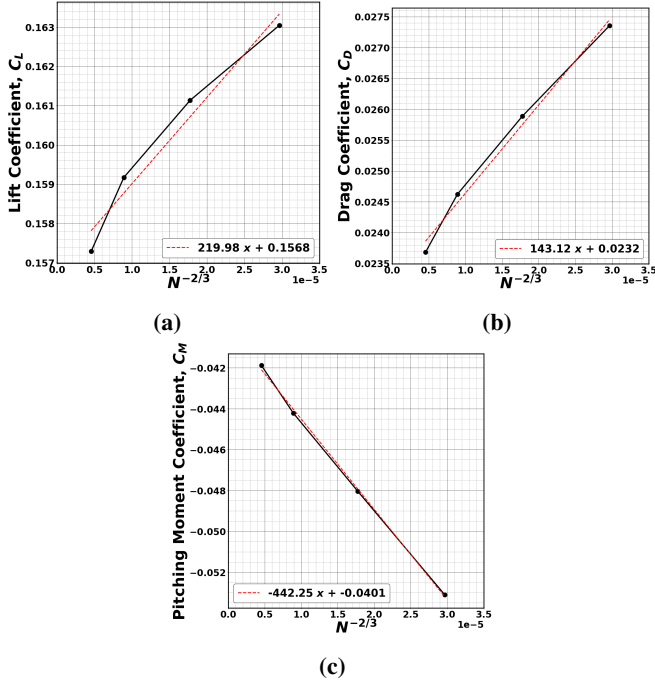


Figure 3: Grid family behavior demonstrated by lift, drag, and pitching moment as a function of grid size (N) for the Baseline configuration. (a) Lift coefficient. (b) Drag coefficient. (c) Pitching moment coefficient.

One of the goals of this work is to establish a baseline for the component study, with the ultimate goal of including rotors and blades in future analyses. Performing such studies can be computationally expensive. Thus, to balance the solution quality and computational resource usage, the fine mesh resolution specifications are used for the remainder of this study. This resolution is also comparable to the mesh used by Liu et al. (Ref. 6).

COMPONENT STUDY

A component study was performed to investigate the effect of the additional features of the vehicle on the aerodynamic performance. The main components of interest are the pylons and landing gears and their effects on the baseline fuselage. The configurations studied in this work are: (1) Baseline (fuselage, wings, empennage), (2) Baseline + Landing Gears (LG) only, (3) Baseline + Pylons only, and (4) Baseline + Landing Gears + Pylons. These configurations enable the consideration of the effect of each set of components separately. In this study, “Landing Gears” refer to the front and rear landing gears, and “Pylons” refer to both the inboard and outboard pylons on both wings.

Updates to the Automatic Meshing Tools In the time between the grid resolution study and the component study, recent developments within the automatic meshing tools had occurred that enabled reduction of manual grid repair effort. These improvements consisted of:

1. Improved turning angle checks to ensure the max turning angle criterion is satisfied.
2. Improved automatic surface grid spacing determination at concave and convex surface features for robust hyperbolic volume mesh generation.
3. Automatic output of X-ray hole-cut instructions for OVERFLOW.

These improvements resulted in grids that differ in final local refinement of features and grid stretching. However, it should be noted that the regions targeted for local refinement on the vehicle surface were largely identical to the grids used in the refinement study. To ensure the fine-mesh parameters outlined in Table 2 were still appropriate, the Baseline case at the Fine-mesh resolution was regenerated and recomputed.

Table 4: The effect of auto-mesh improvements on the baseline mesh and aerodynamics.

	# of NB pts.	C_L	C_D	C_M
Old Baseline	32.8M	0.159	0.0246	-0.0442
New Baseline	37.4M	0.151	0.0276	-0.0442

Table 4 summarizes the comparison of the mesh count and aerodynamic loads for the Baseline mesh with fine resolution parameters before and after the aforementioned improvements. Interestingly, the increase in the near-body resolution has resulted in a 5-10% change in the lift and drag coefficients, while the pitching moment coefficients remain largely the same. A finer-grained breakdown of the contributions to the changes in forces and moments from the integration surfaces of each baseline component (e.g. fuselage, wings, tail, etc.) indicates possible sources of the discrepancy. Table 5 shows the contributions to the changes in loads for each component. In the case of the lift and drag, it can be observed that most of the change is largely due to the fuselage, along with a smaller contribution from the right horizontal tail. Other components, on the other hand, show minor changes in lift, and very little change in drag. It is also interesting to note the changes that occur in the moment coefficient, which appears to be contained mostly in the fuselage and empennage components. This suggests that the increase in resolution is capturing some additional interactions between the fuselage and the tail region. It is possible that more of the turbulent effects from the recirculation region underneath the empennage are being resolved, which can affect downstream components and result in the asymmetric loading observed in the horizontal tails. This phenomena may be related to the limitations of the turbulence model due to the presence of the recirculation behind the fuselage and the bluntness of the fuselage itself. As such, further investigation of this phenomena is beyond the scope of the current study, and the comparison is deemed sufficient due to the reasonable agreement in loads from the other components.

Table 5: The contribution of each Baseline component to the changes in forces and moments. Note that Δ indicates the differences from the old Baseline to the new Baseline results.

Components	ΔC_L	ΔC_D	ΔC_M
Fuselage	0.0084	-0.0030	-0.0094
Right Wing	0.0011	0.0000	-0.0010
Left Wing	0.0018	-0.0002	-0.0010
Vert. Tail	0.0000	0.0000	0.0001
Left Horiz. Tail	0.0005	0.0001	-0.0020
Right Horiz. Tail	-0.0034	0.0002	0.0134
Total	0.0085	-0.0029	0.0000

Meshing of the Tested Configurations For this study, the fine mesh resolution parameters from Table 2 were then utilized to generate the meshes for the different configurations.

Figure 4 shows the surface meshes of the different configurations. Table 6 illustrates the turn around time for mesh generation. This generally includes the time needed for automatically generating meshes, performing manual mesh repairs and mesh connectivity, and defining the integration surfaces. The turn around time mostly consists of mesh repairs and setting up grid connectivity. For example, for the Baseline+LG case, surface and volume meshes were generated with a near-body grid count of 173 in a little under two hours. This also includes time for volume mesh loose coupling, where the near-body meshes are iteratively generated such that the surface mesh connectivity is preserved in the normal marching direction. Manual repairs were required for 34 volume meshes (approximately 20% of the total), where 27 volume meshes had negative Jacobians and 7 volume meshes had self-intersections. For these 34 meshes, 19 of them required surface mesh declustering at the concave corners. Such mesh repair required approximately 1.5 days of manual effort (1 day here represents 1 working day, or approximately 8 hours). Connectivity required an additional four days of ef-

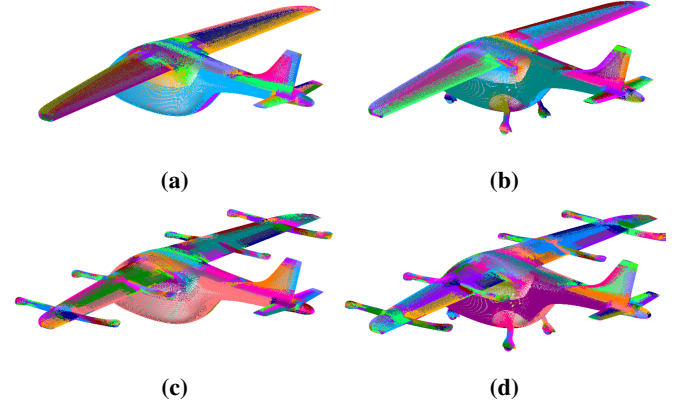


Figure 4: L+C configurations under study. (a) Baseline. (b) Baseline + Gears. (c) Baseline + Pylon. (d) Baseline + Gears + Pylons.

fort. This includes 1.5 days to generate the X-ray maps and 2.5 days to set the proper hole-cut instructions. As part of the orphan point reduction step, additional 10 volume meshes required manual splay adjustment and 12 surface meshes required manual extension or retraction to enforce appropriate overlap with neighboring meshes. The final day in the turn around time was dedicated to improve the force/moment integration hybrid surface definition that was initially generated with the automesh tools. Recent advances in the automation software that occurred after the completion of the current work have removed the need for most of the manual mesh repair work on negative Jacobian removal and mesh overlap enhancement mentioned above. Details of this work will be given in (Ref. 22).

With additional components, the number of near-body surface meshes, and therefore turn-around time, increases. Table 6 shows that going from the Baseline case to the Baseline+LG and the Baseline+Pylons cases adds three days to the turn around time. Using the same X-ray maps and cut-

Table 6: Comparison of grid and computation work for each configuration. The penultimate column details the Standard Billing Unit (SBUs) required to compute these RANS solutions. The SBU is a standard used by the NASA High-End Computing Capability (HECC) for measuring the quantity of computational work across different architectures.

	# of near-body meshes	# of points	Mesh prep. time	SBUs	Iterations
Baseline	106	42.2M	5 work days	358	100K
Baseline + LG	173	72.0M	8 work days	610	100K
Baseline + Pylons	307	93.7M	8 work days	760	100K
Baseline + LG + Pylons	380	107M	8 work days	1461	129K

ting instructions from the Baseline+LG and Baseline+Pylons cases allowed the turn around time to stay at eight days for the Baseline+LG+Pylons case. Without the component buildup approach one would expect the turn around time for the Baseline+LG+Pylons case to increase by about three days. While the turn around time for the automatic surface and volume mesh generation is about a day and half at most for these cases, a fully manual grid setup is expected to take about two weeks for the Baseline case and about three weeks for the other three cases. It is important to note that the automatic meshing tools are reducing the manual effort for surface and volume mesh generation significantly such that the work of weeks is now done in about a day. Automation of volume mesh domain connectivity are in progress and will be addressed in future studies.

The last two columns in Table 6 also indicate the computational effort needed to compute converged flow solutions for each configuration. The quantity of Standard Billing Units (SBUs) appear to scale roughly with the increase in grid size as more components of the configurations are included in the flow computation. The increased jump in SBUs for the full configuration are likely due to a combination of the increased grid size and greater number of iterations required to converge the solution.

Flow Computations at Cruise Using the same flow conditions, RANS simulations are performed for the four configurations of interest. Figure 5 shows the residual convergence for the four test cases. Each case exhibits at least a 6-order drop in residual magnitude. The force and moment coefficients were also confirmed to vary less than a specified range (< 0.001 for C_L , and < 1 drag ct for C_D). As indicated earlier in Table 6, more iterations were required to converge the full configuration.

Table 7 outlines the aerodynamic load variations as various components are added to the baseline configuration. The effect of including the landing gears increases the drag coefficient, which was expected. It is also interesting to observe the slight increases in lift and pitching moment coefficients as well. The addition of the pylons resulted in a reduction in the lift coefficient. This was also expected, since the pylons can disturb the suction effect that occurs at the leading edge of the main wings. The decrease in lift also resulted in an anticipated increase in drag. This drag can be attributed to several factors, such as the form and interference drag of the pylons, and from the reduced effect of the favorable pressure gradient over the

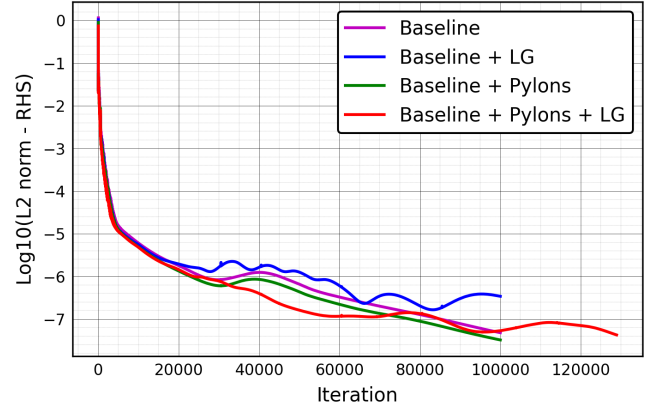


Figure 5: Evolution of solution L2-norm residual for the various L+C configurations.

suction regions of the main wing leading-edge. Overall, the landing gears affect the lift, drag, and pitching moment coefficients by around 3-8%, while the pylons have a larger effect on those loads by nearly 20-30%.

The effect of including all the components to the baseline configuration on the change in the force and moment coefficients appears to exhibit almost a superposition effect of each individual set of components. There appears to be a consistent 8-10 “counts” discrepancy across all loads, which may suggest some minor interaction effects between all the various components. This can also be due to some minor differences in the gridding of each geometry, since the automatic meshing scheme generates them independently of each other.

Another interesting aspect to note are the roll and yaw moment coefficients ($C_{L_{roll}}$ and C_N , respectively). In all cases, the geometries are generally symmetric and should not exhibit particularly large roll or yaw moments. The results, however, indicate that the cases with the landing gears have much smaller roll and yaw moments than the configurations without landing gears. The large percentage differences of the roll and yaw moment coefficients are due to the small loading at straight and level flight. As discussed earlier with the comparison between the new and old Baseline meshes and solutions, it is possible that this can be attributed to the increased resolution of certain wakes and recirculation regions. The presence of the landing gears also appears to delay the asymmetric behavior further downstream closer to the tail region.

Figure 6 shows the contours of the surface pressure coeffi-

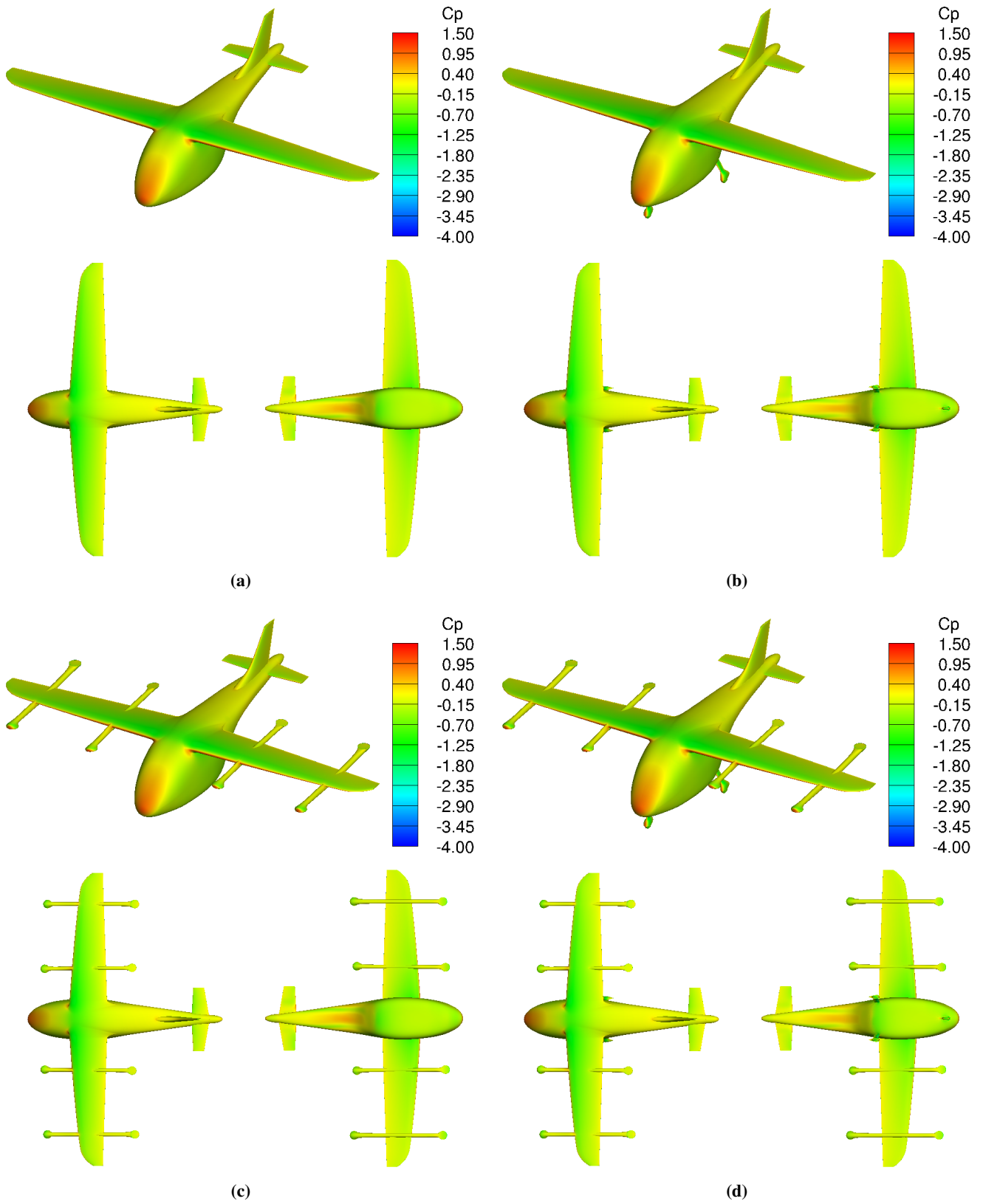


Figure 6: Surface pressure coefficient contours of the various L+C configurations under study. Each figure shows an isometric view (top), a top view (left), and a bottom view (right). (a) Baseline. (b) Baseline + LG. (c) Baseline + Pylons. (d) Baseline + LG + Pylons.

Table 7: Component build-up on aerodynamic loads and moments. Here, Δ indicates the difference of each configuration from the Baseline case.

	C_L	ΔC_L	C_D	ΔC_D	C_M	ΔC_M
Baseline	0.1507	—	0.0276	—	-0.0442	—
Baseline + LG	0.1593	+0.0086 (+5.71%)	0.0284	+0.0008 (+2.96%)	-0.0409	+0.0033 (+7.42%)
Baseline + Pylons	0.1245	-0.0262 (-17.4%)	0.0327	+0.0051 (+18.6%)	-0.0301	+0.0141 (+31.9%)
Baseline + LG + Pylons	0.1315	-0.0192 (-12.7%)	0.0328	+0.0052 (+18.8%)	-0.0276	+0.0166 (+37.6%)

	$C_{L_{roll}}$	$\Delta C_{L_{roll}}$	C_N	ΔC_N
Baseline	0.0093	—	-0.0112	—
Baseline + LG	0.0004	-0.0089 (-95.2%)	0.0010	+0.0122 (+109%)
Baseline + Pylons	0.0088	-0.0005 (-5.36%)	-0.0105	+0.0007 (+6.21%)
Baseline + LG + Pylons	0.0014	-0.0079 (-85.1%)	-0.0004	+0.0108 (+96.2%)

cient for each of the tested configurations. Common stagnation regions can be observed at the nose of the fuselage and the leading edges of the various lifting surfaces. The added components also exhibit stagnation regions on the aft-most regions. On the underside of the vehicle, a higher-pressure region can be observed underneath the empennage. Figure 7

provides a closer look at how the inclusion of the pylons affects the flow on the wing. Figures 7a and 7c show cuts near the inboard and outboard pylons, respectively, while Figure 7b shows a constant-span cut halfway between the two pylons on the wing. In general, the pylons appear to reduce the suction peaks over the leading edge. Away from the pylons, the effect is not as pronounced, but is still present. Figure 7d shows a span-wise cut of the surface pressures. An increase in pressures on both the upper and lower surfaces of the wing can be observed at the pylon intersection regions. It can also be observed that the pylons reduce the overall pressure differential between the upper and lower surfaces.

Figure 8 shows the surface skin friction for the four configurations considered. In all cases, it can be observed that there is a recirculation region underneath the fuselage just forward of the empennage and aft of where the landing gears join the fuselage. There is also an increase in skin friction from the flow negotiating around where the pylons intersect the leading edge of the wing. It appears that the pylons do not induce any separation over the wing at level flight. There appears to be separation underneath the pylons at the location of the forward rotors. However, this is likely due to the fact that a flat face has been left where the rotor hubs would normally join the pylons. In the case of the landing gears, the flows appear to be largely attached for the fairings. At the junctions between the fairings to the fuselage, there also appears to be corner separation near the trailing edges. Some small corner separation can also be observed where the pylons join the wing in the trailing-edge region. However, a proper analysis of these separation regions will require a solution computed with a RANS model that also incorporates the quadratic constitutive relation.

CONCLUSION

This work is motivated to address the effects of various L+C components on aerodynamic forces and moments while demonstrating the capability of the automatic meshing tools for performing rapid computational analysis and generating quality computational results. Utilizing automatic meshing tools, a grid refinement study was performed on the baseline configuration. Through comparison of integrated aero-

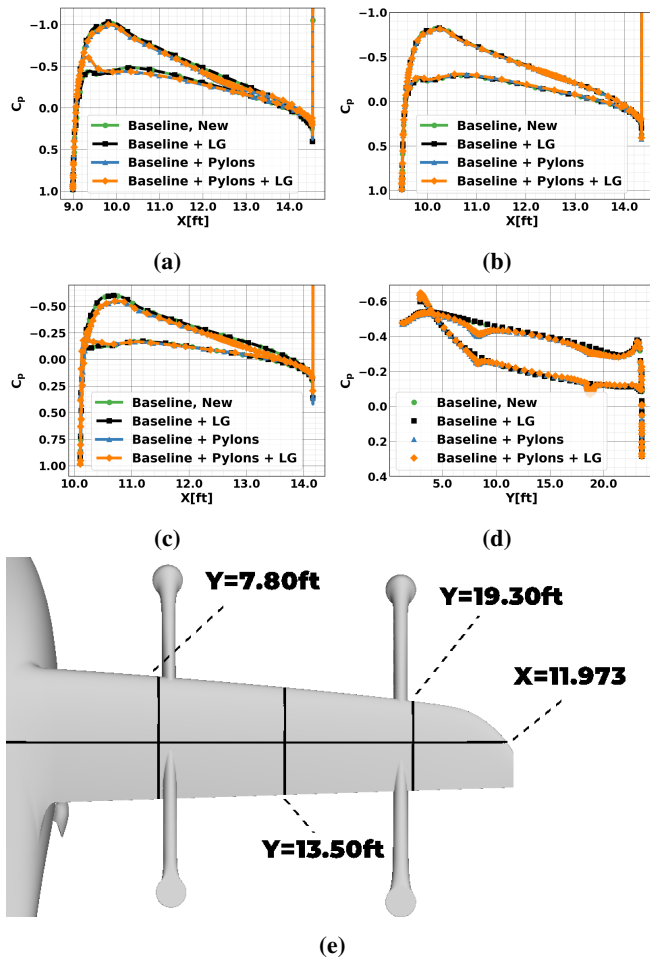


Figure 7: Surface pressure cuts on the right wing for each configuration. (a) $Y = 7.80$ ft. (b) $Y = 13.5$ ft. (c) $Y = 19.3$ ft. (d) $X = 11.973$ ft. (e) Locations of C_p cuts.

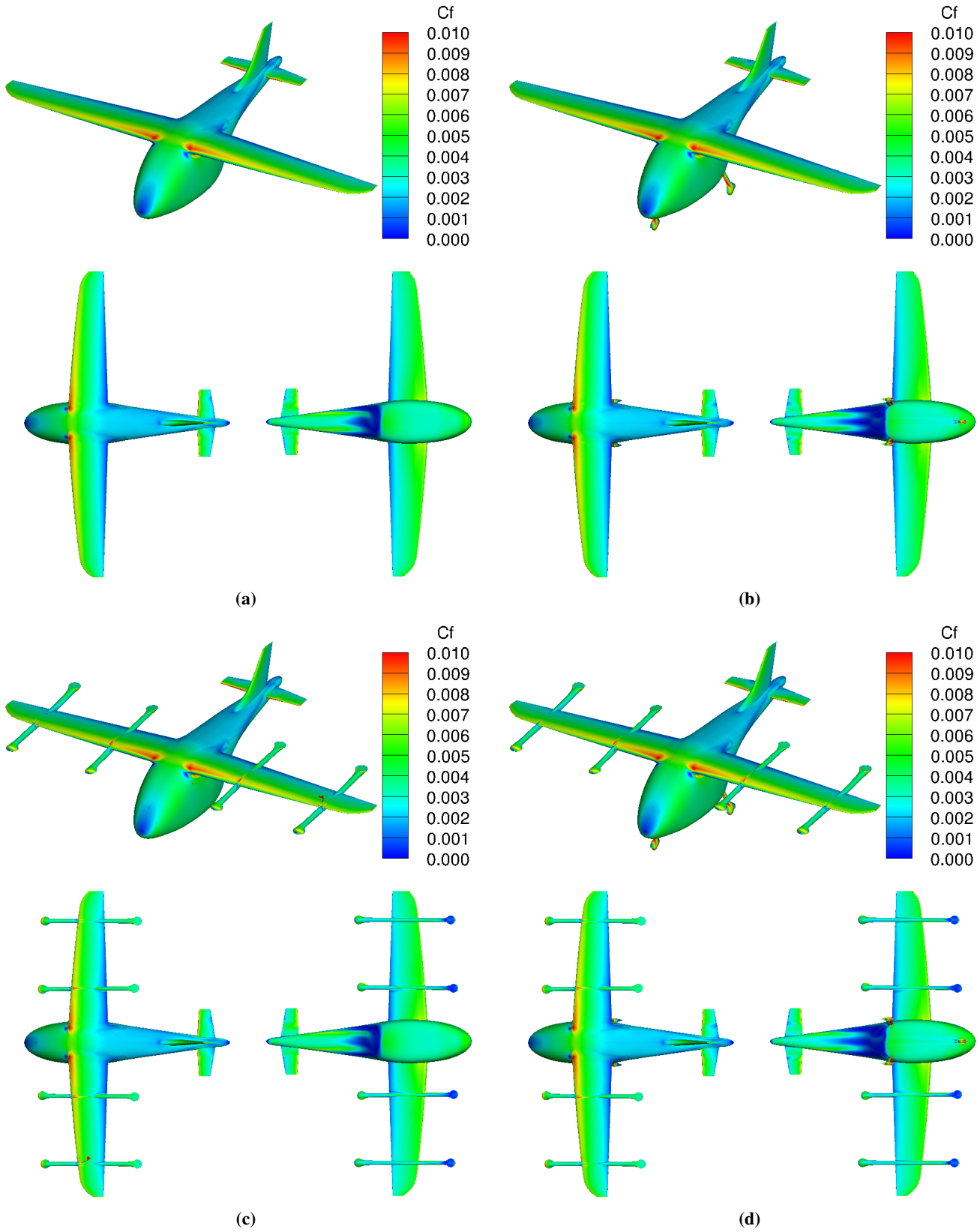


Figure 8: Surface skin-friction coefficient contours of the various L+C configurations under study. Each figure shows an isometric view (top), a top view (left), and a bottom view (right). (a) Baseline. (b) Baseline + LG. (c) Baseline + Pylons. (d) Baseline + LG + Pylons.

dynamic loads and convergence behavior, the automatic tools were shown capable of generating a family of meshes with consistent refinement.

The automatic meshing tools were then applied to investigate the effect of incorporating the pylons and landing gears on the vehicle aerodynamics. An incremental analysis was performed where each component was individually incorporated into the baseline configuration and analyzed before all components were incorporated together in the full case. This resulted in four geometries that were analyzed. Overall, we are able to obtain a relatively quick turnaround time to generate each geometry with the speed-up available from the automatic overset meshing tools. The analysis showed that the global effect of each set of components exhibits a near superposition-like quality on the integrated load coefficients. As expected, the pylons appear to reduce the lift of the configuration due to interference with the leading-edge suction region, and both the pylons and landing gears also increase the overall drag of the vehicle.

Future work will consider the currently missing components of the vehicle analysis. This mainly consists of the lifting rotors and the rear tail propeller. In the cruise portion of the flight, the lifting rotors will be held in a fixed position and, as such, should be relatively straightforward to include. Addition of the tail propeller, however, will require an unsteady solution with relative motion. It will be necessary to consider using unsteady RANS or even detached eddy simulation. In addition to increasing the fidelity of the geometry, future efforts may also consider investigating the use of QCR with the current turbulence model. The inclusion of more components to the baseline introduces more corner-type separation, and QCR may be necessary to properly resolve such flows. In the case of automatic meshing, future efforts will be focused on continuing to reduce the turn-around time that is currently possible when attempting to generate a structured overset mesh from a BRep solid model. Such efforts will be mainly focused on reducing the manual effort needed to setup a case once the automatic meshing tools generate a near-body volume mesh, such as the repair times and computing connectivity.

Author contact:

S. Sheida Hosseini seyedeh.sheida.hosseini@nasa.gov

Andrew M. Chuen andrew.m.chuen@nasa.gov

William M. Chan william.m.chan@nasa.gov

ACKNOWLEDGEMENTS

This work is funded by NASA's Revolutionary Vertical Lift Technology (RVLT) and Transformational Tools and Technologies (TTT) projects. Computational resources have been provided by the NASA Advanced Supercomputing (NAS) facility at NASA Ames Research Center. The authors would also like to thank Dr. Tom Pulliam for insightful discussions on running these test cases using OVERFLOW.

REFERENCES

1. Antcliff, K. R., Moore, M. D., and Goodrich, K. H., "Silicon valley as an early adopter for on-demand civil VTOL operations," Paper AIAA 2016-3466, 16th AIAA Aviation Technology, Integration, and Operations Conference, Washington, D.C., June 13–17, 2016. DOI: 10.2514/6.2016-3466.
2. Johnson, W., and Silva, C., "NASA concept vehicles and the engineering of advanced air mobility aircraft," *The Aeronautical Journal*, Vol. 126, (1295), January 2022, pp. 59–91. DOI: 10.1017/aer.2021.92.
3. Silva, C., Johnson, W. R., Solis, E., Patterson, M. D., and Antcliff, K. R., "VTOL Urban Air Mobility Concept Vehicles for Technology Development," Paper AIAA 2018-3847, 18th AIAA Aviation Technology, Integration, and Operations Conference Proceedings, Atlanta, GA, June 25–29, 2018. DOI: 10.2514/6.2018-3847.
4. Johnson, W., and Silva, C., "Observations from Exploration of VTOL Urban Air Mobility Designs," Paper AIAA 2000-2013, 7th Asian/Australian Rotorcraft Forum, Jeju Island, Korea, October 30–November 1, 2018.
5. Bacchini, A., Cestino, E., Van Magill, B., and Verstraete, D., "Impact of lift propeller drag on the performance of eVTOL lift+cruise aircraft," *Aerospace Science and Technology*, Vol. 109, February 2021, pp. 106429. DOI: 10.1016/j.ast.2020.106429.
6. Liu, Y., Druyor, C. T., and Wang, L., "High-fidelity Analysis of Lift+Cruise VTOL Urban Air Mobility Concept Aircraft," Paper AIAA 2023-3671, AIAA Aviation 2023 Forum, San Diego, CA, June 12–16, 2023. DOI: 10.2514/6.2023-3671.
7. Anderson, W. K., Biedron, R. T., Carlson, J.-R., Derlaga, J. M., T., D. C., Jr., P. A., Gnoffo, Hammond, D. P., Jacobson, K. E., Jones, W. T., Kleb, B., Lee-Rausch, E. M., Nastac, G. C., Nielsen, E. J., Park, M. A., Rumsey, C. L., Thomas, J. L., Thompson, K. B., Walden, A. C., L., W., Wood, S. L., Wood, W., Diskin, B., Liu, Y., and Zhang, X., "FUN3D Manual: 14.0," NASA TM 20220017743, 2022.
8. Johnson, W., "Rotorcraft Aerodynamic Models for a Comprehensive Analysis," American Helicopter Society 54th Annual Forum, Washington, D.C., May 20–22, 1998.
9. Ventura Diaz, P., Caracuel Rubio, R., and Yoon, S., "Simulations of ducted and coaxial rotors for air taxi operations," Paper AIAA 2019-2825, 6th AIAA/CEAS Aeroacoustics Conference, Dallas, TX, June 17–21, 2019. DOI: 10.2514/6.2019-2825.
10. Ventura Diaz, P., Johnson, W., Ahmad, J., and Yoon, S., "The Side-by-Side Urban Air Taxi Concept," Paper AIAA 2019-2828, AIAA Aviation 2019 Forum, Dallas, TX, June 17–21, 2019. DOI: 10.2514/6.2019-2828.
11. Ventura Diaz, P., and Yoon, S., "High-fidelity Simulations of a Quadrotor Vehicle for Urban Air Mobility,"

- Paper AIAA 2022-0152, 2022 AIAA Science and Technology Forum and Exposition, San Diego, CA, January 3–7, 2022. DOI: 10.2514/6.2022-0152.
12. Garcia Perez, D., Ventura Diaz, P., and Yoon, S., “High-Fidelity Simulations of a Tiltwing Vehicle for Urban Air Mobility,” Paper AIAA 2023-2282, 2023 AIAA Science and Technology Forum and Exposition, National Harbor, MD, January 21–27, 2023. DOI: 10.2514/6.2023-2282.
 13. Ventura Diaz, P., Garcia Perez, D., and Yoon, S., “Multi-Fidelity Computational Analysis of a Quiet Single-Main Rotor Helicopter for Air Taxi Operations,” Paper AIAA 2023-3669, AIAA Aviation 2023 Forum, San Diego, CA, June 12–16, 2023. DOI: 10.2514/6.2023-3669.
 14. Chan, W. M., Pandya, S. A., and Haimes, R., “Automation of Overset Structured Surface Mesh Generation on Complex Geometries,” Paper AIAA 2019-3671, AIAA Aviation 2019 Forum, Dallas, TX, June 17–21, 2019. DOI: 10.2514/6.2019-3671.
 15. Chan, W. M., Pandya, S. A., and Chuen, A. M., “Automation of Overset Structured Mesh Generation on Boundary Representation Geometries,” Paper AIAA 2022-3607, AIAA Aviation 2022 Forum, Chicago, IL, June 27– July 1, 2022. DOI: 10.2514/6.2022-3607.
 16. Chuen, A. M., Hosseini, S. S., Jensen, J. C., and Chan, W. M., “Aerodynamic Simulations for Complex Geometries Using Automatically Generated Structured Overset Meshes,” Paper AIAA 2023-3602, AIAA Aviation 2023 Forum, San Diego, CA, June 12–16, 2023. DOI: 10.2514/6.2023-3602.
 17. Derlaga, J. M., Jackson, C. W., and Buning, P. G., “Recent Progress in OVERFLOW Convergence Improvements,” Paper AIAA 2020-1045, 2020 AIAA Science and Technology Forum and Exposition, Orlando, FL, January 6–10, 2020. DOI: 10.2514/6.2020-1045.
 18. Chan, W., Gomez, R., Rogers, S., and Buning, P., “Best Practices in Overset Grid Generation,” Paper AIAA 2002-3191, 32nd AIAA Fluid Dynamics Conference and Exhibit, St. Louis, MO, June 24–26, 2002. DOI: 10.2514/6.2002-3191.
 19. Haimes, R., and Dannenhoffer, J., “The Engineering Sketch Pad: A Solid-Modeling, Feature-Based, Web-Enabled System for Building Parametric Geometry,” Paper AIAA 2013-3073, 21st AIAA Computational Fluid Dynamics Conference, San Diego, CA, June 24–27, 2013. DOI: 10.2514/6.2013-3073.
 20. Meakin, R., “Object X-rays for cutting holes in composite overset structured grids,” Paper AIAA 2001-2537, 15th AIAA Computational Fluid Dynamics Conference, Anaheim, CA, June 11–14, 2001. DOI: 10.2514/6.2001-2537.
 21. Hensch, M. J., “Statistical Analysis of Computational Fluid Dynamics Solutions from the Drag Prediction Workshop,” *Journal of Aircraft*, Vol. 41, (1), 2004, pp. 95–103. DOI: 10.2514/1.1796.
 22. Chan, W. M., and Chuen, A. M., “Advances in Automation of Structured Overset Volume Mesh Generation and Domain Connectivity,” Abstract submitted, AIAA Aviation 2024 Forum, Las Vegas, NV, 2024.